Chemical Engineering Journal 498 (2024) 155363

Contents lists available at ScienceDirect

Chemical Engineering Journal

journal homepage: www.elsevier.com/locate/cej

Laser driven generation of single atom Fe-N-C catalysts for the oxygen reduction reaction

Ainhoa Madrid [a,b,c], Álvaro Tolosana-Moranchel [d], Álvaro García [d], Sergio Rojas [d,*], Fernando Bartolome [e], Ekaterina Pakrieva [a,b,c], Laura Simonelli [f], Gema Martinez [a,b,c,g,*], Jose L. Hueso [a,b,c,h,i,*], Jesus Santamaria [a,b,c,i,*]

[a] Instituto de Nanociencia y Materiales de Aragon (INMA) CSIC-Universidad de Zaragoza, Campus Rio Ebro, Edificio I+D, C/ Poeta Mariano Esquillor, s/n, 50018 Zaragoza, Spain
[b] Department of Chemical and Environmental Engineering, University of Zaragoza, Campus Rio Ebro, C/María de Luna, 3, 50018 Zaragoza, Spain
[c] Networking Research Center on Bioengineering, Biomaterials and Nanomedicine (CIBER-BBN), 28029 Madrid, Spain
[d] Grupo de Energía y Química Sostenibles, Instituto de Catálisis y Petroleoquímica, CSIC. Marie Curie 2, 28049 Madrid, Spain
[e] Departamento de Física de la Materia Condensada, Universidad de Zaragoza, 50009 Zaragoza, Spain
[f] CELLS–ALBA Synchrotron, E-08290 Cerdanyola del Vallès, Barcelona, Spain
[g] Centro Universitario de la Defensa (CUD), Ctra. de Huesca 50090 Zaragoza, Spain
[h] Escuela Politécnica Superior, Universidad de Zaragoza, Crta. de Cuarte s/n, 22071, Huesca, Spain
[i] Instituto de Investigación Sanitaria (IIS) de Aragón, Avenida San Juan Bosco, 13, 50009 Zaragoza, Spain

ARTICLE INFO

Keywords:
Laser pyrolysis
Single Atom Catalysts
ORR
Fe-N
Phthalocyanines
Carbon

ABSTRACT

Single-Atom Catalysts (SACs) have emerged as the ultimate solutions in challenging systems bridging the gap between homogeneous and heterogeneous catalysts. However, feasible synthesis methods are necessary to stabilize single metal atoms, increase catalyst loadings and scale up the synthesis. Due to its sluggish kinetics, the oxygen reduction reaction (ORR) is the main source of irreversibility in proton exchange membrane fuel cells (PEMFC). The most promising candidates to replace Pt-based catalysts for the ORR in fuel cells are the so-called Fe-N/C catalysts. These catalysts display high ORR activity in acidic and alkaline electrolytes. In this work, we propose a laser-driven pyrolysis approach to generate Fe-N/C SACs that involves decomposition of aerosolized iron-phthalocyanines. The resulting catalyst displays ORR activity in acidic and alkaline electrolytes, with competitive half-potential and kinetic current density values in comparison with state-of-the-art electrocatalysts.

1. Introduction

Single-Atom Catalysts (SACs) with catalytically active metal dispersed as exclusively discrete atoms, have recently emerged as the ultimate solution for overcoming the limitations of traditional catalysts by bridging the gap between homogeneous and heterogeneous catalysts [1–7]. Atomically dispersed active sites enable a maximal atomic utilization; every metal atom can theoretically participate in the catalytic reactions as an active site, which eventually increase the mass activity of the metal element and turnover frequency of the reaction. To date, numerous SACs dispersed on various supports (such as metal oxides or carbon-based matrix) have been reported [4–10]. Carbon-based SACs often containing transition-metal-nitrogen-carbon entities M−N/C (M typically refers to Fe, Ni, Cu, Ti, Co or Mn), rank among the most promising and environmentally friendly alternatives, due to their competitive catalytic activity in electrochemical reactions including, oxygen reduction reaction (ORR), hydrogen evolution reaction (HER), and CO_2 electroreduction reaction [4–7,10–15]. Despite the tremendous potential of SACs and the progress made in the last decade, key challenges remain unsolved as highlighted in recent review articles [4–7,10,16]. First, stabilizing single metal atoms is extremely difficult due to the preferential aggregation of metal atoms [17]. This leads to very low catalyst loadings: As the metal loading increases, the preference is to form clusters or nanoparticles, instead of single atom sites.

* Corresponding authors at: Instituto de Nanociencia y Materiales de Aragon (INMA) CSIC-Universidad de Zaragoza, Campus Rio Ebro, Edificio I+D, C/ Poeta Mariano Esquillor, s/n, 50018 Zaragoza, Spain (G. Martinez, J.L. Hueso, J. Santamaria); Grupo de Energía y Química Sostenibles, Instituto de Catálisis y Petroleoquímica, CSIC. Marie Curie 2, 28049 Madrid, Spain (S. Rojas).
E-mail addresses: srojas@icp.csic.es (S. Rojas), gemamar@unizar.es (G. Martinez), jlhueso@unizar.es (J.L. Hueso), jesus.santamaria@unizar.es (J. Santamaria).

https://doi.org/10.1016/j.cej.2024.155363
Received 7 March 2024; Received in revised form 24 July 2024; Accepted 29 August 2024
Available online 31 August 2024

Second, the lack of accurate preparation methods gives rise to"false SACs" where, in addition to dispersed single atoms a variety of species coexist, i.e. subnanometer clusters and nanoparticles with a wide range of sizes [9]. As a result, the catalytic response is diverse and resulting either in a loss of activity and selectivity or in positive responses accompanied of complex catalytic mechanisms yet to unravel [4]. These problems seriously restrict the extensive applications of SACs and therefore a synthesis method, preferentially scalable and able to provide higher catalyst loadings with a dominance of true SAC sites is sorely needed [4]. The synthesis of SACs is a huge challenge due to their high surface free energy and preferential aggregation of metal atoms. Traditional strategies for nanoparticles (NPs) under hydrothermal environments or high temperature easily lead to the Oswald ripening [9], which are not fit for the synthesis of SACs. Therefore, an intense research effort has been directed to finding methods to create stable SAC sites [4,6,16,18].

In addition, the scalability, the understanding and control of the environment surrounding the metal sites are other factors of paramount importance that must be carefully taken into account in order to accelerate the implementation of SACs [4,10,19]. The synthesis of SACs in a view of atomically substantial strategy design can be divided into two main strategies based on the key process during the synthesis: trapping or implantation-confinement. The key challenge in the former is to trap active metal atoms in the support by: defect trapping, ligand trapping or surface dangling bond trapping to achieve a substrate supported single atom structure. Essentially, the usual bulk transformation methods; [20,21], atomic layer deposition [22], galvanic replacement [23] and M−precursors pyrolysis methods can be included in the trapping strategy [24]. Although some of these methods have provided good results for specific systems, in general, they are not applicable to a wide variety of SACs, require sophisticated preparation procedures and give low yields per batch. In addition, they are intrinsically difficult to scale up, both in terms of increasing the metal loading and of developing continuous preparation processes. Thus, large-scale production seems unattainable, hindering their potential use in practical applications [4].

To overcome the above-discussed problems of trapping strategies, implantation-confinement strategies have emerged. These involve cage anchoring to restrict the migration of metal atoms. Template-removal methods [25] and metal–organic-frameworks (MOFs) transformation methods [26], belong to this strategy. Thus, since the pioneer Li and Wu's work [27,28], high-temperature pyrolysis of MOFs have been extensively employed for the fabrication of metal-supported N-doped carbon materials [4,28–30]. This strategy not only yield metal loading substantially above 1 %, but also higher stability compared to SACs synthesized by other methods. Their main disadvantage relates to the need to synthesize the MOF precursors, a synthesis generally expensive and often tedious and un-amenable to continuous, scaled-up production. This is even clearer for alternative methods involving the use of sacrificial templates [4,31,32], where the cost penalty of synthesizing a sophisticated template and then destroying it makes the process economically unfeasible, not to mention the fact that the template-removal process is likely to damage the structure of the SAC material and may introduce impurities. Despite the above remarkable disadvantages, metal-supported N-doped carbon materials are currently highly promising substitutes for Pt-based materials, towards oxygen reaction reduction (ORR) in both alkaline and acidic electrolytes through a four-electron pathway [4–7,11,13,18,27,30,33–36]. The most appealing candidates are Fe, Co and Ni, and of these, Fe-N/C materials possess superior ORR electrocatalytic activity, even approaching to that commercial Pt/C [4,36,37].

In this work, we propose a laser-driven pyrolysis approach to produce SACs that also involves decomposition of suitable precursors, but avoids most of the above-mentioned problems. Laser pyrolysis is a well-established technology for the generation of nanomaterials and coatings with a high degree of control on composition or purity [38–40]. The use of continuous wave CO_2 laser sources warrant elevated heating rates, high reaction temperatures and short reaction times [38]. Laser pyrolysis has been traditionally exploited for the generation of nanopowders with optical, magnetic and biomedical applications [38,41–43]. In recent years, this technique is gaining an increasing interest for the development of carbon-based materials devoted to energy applications and it is also expanding its potential for the generation of hybrid materials [38,42]. We leverage some of these intrinsic characteristics of the laser pyrolysis process (instantaneous heating, well defined reaction zone, immediate quenching of temperature and reaction beyond the laser spot) and add a novel feature beyond the current-state-of-the-art in laser-driven reactors, including a new aerosol feeding system. Remarkably, the generation of aerosols allows the use of affordable solid precursors that can be conveniently re-suspended and fed into the laser reaction chamber, thereby expanding the plethora of potential alternatives for laser pyrolysis non-previously disclosed for this technique.

The solvent must be carefully selected, since its role is not only to transport the solid metal precursors to the reaction zone, but also is responsible for the in-situ sequestration of the single atoms that will be captured within the carbonaceous matrix. By carefully combining organometallic precursors and solvents, M−N/C SACs with controlled doping of N can be tailored by this approach. The chemical and structural characterization of the synthesized material revealed that the metal atoms were dispersed in an N-doped C matrix. The as-prepared catalysts were further heat treated in a gas atmosphere. This activation process effectively enabled the properties of the particles without destroying the nanoscale structure of the material, keeping intact the metal dispersion as exclusively single atoms. The resulting catalysts displayed high ORR activity in acidic and alkaline electrolytes, with competitive half-potential values, kinetic current densities and turnover frequencies (TOFs) when compared with state-of-the-art electrocatalysts.

2. Experimental

2.1. Laser-driven synthesis of the Fe-N/C catalysts

The synthesis of the catalysts was carried out by laser pyrolysis in a continuous flow reactor described elsewhere [44,45] and with more detail in the Supplementary Materials section. The reactor setup and process is depicted in Fig. 1. Iron phthalocyanine (42 mg) was dissolved in pyridine (25 mL) and the solution was fed from a sealed chamber equipped with a 1.65 MHz nebulizer board, working at 40 V. An infrared CO_2 laser beam (Rofin SCx30, $\lambda = 10.6$ μm) was settled to intersect orthogonally with the aerosol stream. Ammonia was co-fed in certain experimental conditions to maximize the formation of carbon

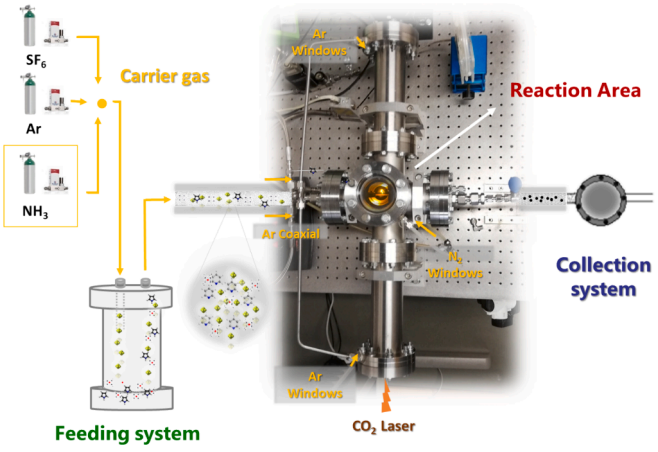

Fig. 1. Illustration of the experimental setup for the synthesis of single atom Fe-N-C catalysts showing the feeding system, the reaction area and the filter collection system.

containing N-C units. The synthesis of these materials was performed by the Synthesis of Nanoparticles Unit (UNIT 9) of the ICTS "NANBIOSIS" at the Institute of Nanoscience and Materials of Aragon (INMA)-Universidad de Zaragoza.

2.2. Catalyst activation

The samples obtained from laser pyrolysis (**Fe-N@C**, and **Fe-N@C-NH_3**) were subjected to a thermal treatment. First, the temperature was raised from room temperature to 900 °C using a 20 °C·min^{-1} ramp under a N_2 flow of 450 NmL·min^{-1}. After 110 min at 900 °C, NH_3 was fed in the reactor (N_2/NH_3 = 450/70 NmL·min^{-1}), for 30 min. Then, the pyrolysis reactor was cooled down to room temperature under flowing nitrogen. These samples were acid leached in 2 M H_2SO_4 during 8 h at 70 °C, in order to remove non-stable iron phases. The solid recovered was subjected to a second pyrolysis under the same temperature program. The catalysts obtained after a second thermal treatment were labelled as **Fe-N@C (2HT)**, and **Fe-N@C-NH_3 (2HT)**, respectively.

2.3. Electrochemical tests

Electrochemical tests were recorded using an Autolab PGSTAT320N potentiostat/galvanostat controlled with the NOVA software. Measurements were performed using a three-electrode set-up. The electrocatalyst under study was deposited on a glassy-carbon electrode (0.196 cm^2) mounted on a rotating disk electrode (RDE) by means of an ink. Before ink deposition, the disk electrode surface was thoroughly cleaned and carefully polished with a micropolish alumina 0.05 μm. The ink was prepared by dispersing the desired amount of catalyst in a mixture of ultrapure water (MilliQ® water 18.2 MΩcm), isopropanol and Nafion 117 solution (5 %) with a volume ratio of 1:1:0.052 to a final concentration of 6 $mg_{cat}·mL^{-1}$. Unless otherwise stated, catalyst loading on the electrode was 0.8 $g_{cat}cm^{-1}_{geom}$. An Ag/AgCl (3 M KCl) electrode (Metrohm) and a graphite rod were used as the reference and counter electrodes, respectively. Potentials are reported vs the reversible hydrogen electrode (RHE) after iR correction. Resistances of 24 and 42 Ω in 0.1 M $HClO_4$ and 0.1 M KOH, respectively, were determined by electrical impedance spectroscopy (EIS) at open voltage.

Prior to each experiment, the potential of the reference electrode was calibrated by recording the potential of the hydrogen evolution reaction using a Pt wire as working electrode [46]. The oxygen reduction reaction (ORR) was measured in both 0.1 M KOH and 0.1 M $HClO_4$ electrolytes. A 0.5 M acetate buffer of pH 5.2 (prepared with sodium acetate and glacial acetic acid) was used as electrolyte for the *in situ* nitrite stripping experiments [47]. Before measuring the ORR, cyclic voltammograms (CVs) at 50 mV·s^{-1} in Ar-saturated electrolyte were collected until a constant response was obtained. For the evaluation of the ORR, the electrolyte was saturated with oxygen and a series of CVs between 0.05 and 1.2 V at 10 mV·s^{-1} at 1600 rpm were recorded until a constant response was obtained. For the determination of the ORR activity, the positive-going currents were used. After the ORR, a blank voltammogram was recorded in Ar-saturated electrolyte at 10 mV·s^{-1} and used for double layer correction.

2.4. XANES and EXAFS characterization

XAS experiments were performed at the BL22 beamline "CLAESS" of the ALBA synchrotron (Barcelona, Spain) [48], using the Si(111) double crystal monochromator. The materials were studied at the Fe K-edge (7.1 keV). XANES and EXAFS spectra were recorded at room temperature in the fluorescence mode. The energy of the absorption spectra was calibrated by measuring the XANES of a Fe metal foil (used as reference in our study) and of several Fe oxides in transmission mode. For the measurements, both pellets and homogeneous layers of powdered samples were used. Powdered samples were made by spreading fine powders of the material onto an adhesive Kapton tape. The samples were measured in fluorescence mode at room temperature, using a full plastic sample holder. The sample vacuum chamber was aluminum-based to avoid any artifactual counts from scattered beams on the chamber. The absorption spectra were analyzed according to standard procedures [49,50] by using the Demeter-IFEFFIT program package [51]. A complete discussion of the procedure can be found elsewhere [52,53]. It should be noted that the measurements showed no modification of the XAS spectra along several hours of measurement, indicating that the observed properties are intrinsic and stable in time, that is, no beam damage was observed in any of the specimens.

3. Results and discussion

3.1. Preparation of atomically dispersed Fe-N/C nanomaterials

The single atom catalysts (SACs) were synthesized by laser pyrolysis (see Experimental section and Supplementary materials for further details). It consists of an aerosol generator filled with a solution of iron phthalocyanine in pyridine, connected to the laser pyrolysis reactor. The actual size range of droplets generated by this unit was measured by a laser particle size analyser. The size profile of the solution differs from that of the pure solvent, which is centered at 7 μm (Figure S1). In the process of CO_2 laser pyrolysis, the first stage is the laser excitation process. Sulfur hexafluoride (SF_6) was used as photosensitizer to accomplish the energy transfer process between the laser light and the precursor solution. The molecular mechanism involves the resonant absorption of photons by IR-active vibrational energy modes of the acceptor (SF_6) in ground electronic state. The energy transferred on the exchange of vibrational energy of the SF_6 molecules to translational energy was used to heat the total volume of the droplets transported in the carrier gas. Such local superheating-induced droplet destruction was often accompanied by the appearance of a flame in the interaction volume. The droplets rapidly disassemble into small molecular fragments or even atoms. Because of the sudden and abrupt decline of temperature with radial distance, product condensation starts abruptly, resulting in a spray of nanoparticles. The freshly solid materials were directly collected into a cellulose filter supported onto a stainless-steel reservoir. The samples obtained by pyrolysis of iron phthalocyanine in pyridine were labeled as **Fe-N@C** and **Fe-N@C-NH_3** to distinguish the absence or presence of an additional co-feeding of NH_3, respectively. In order to enhance their catalytic activity, an activation step of the as-prepared solids was carried out. Typically, activation sequence included (i)-heat treatment- (ii) acid etching- (iii) 2nd heat treatment [54,55]. The catalysts after the activation treatment were identified as **Fe-N@C(2HT)** and **Fe-N@C-NH_3(2HT)**, respectively.

3.2. Characterization of Single-Atoms catalysts

The morphological features of the samples directly obtained from the pyrolysis process (**Fe-N@C** and **Fe-N@C-NH_3)** were characterized by high-resolution transmission electron microscopy (HR-TEM). As shown in Fig. 2, the particles collected after laser pyrolysis formed aggregates containing smaller interconnected carbon particles. The particle size distribution revealed mean diameters for primary particles of approximately 20 nm in both samples (Fig. 2a and 2d). TEM images showed no evidence of large iron-based nanoparticles. It was also observed that the carbon networks were mostly disordered in the **Fe-N@C** sample (Fig. 2b-2c) and exhibited some onion-like domains in the **Fe-N@C-NH_3** (Fig. 2e-2f) and samples. Clearly, this fact leads to the turbostratic stacking of graphite planes (Fig. 2f) in this latter sample [56,57].

High-angle annular dark-field scanning transmission electron microscopy (HAADF-STEM) and energy-dispersive X-ray spectroscopy (EDS) mapping confirmed the homogeneous distribution of elements, especially the Fe atoms (Fig. 3). Fig. 3a and Fig. 3e revealed a uniform dispersion of C, N and Fe over the whole architecture of samples **Fe-N@C** and **Fe-N@C-NH_3**, respectively. The aberration corrected HAADF-

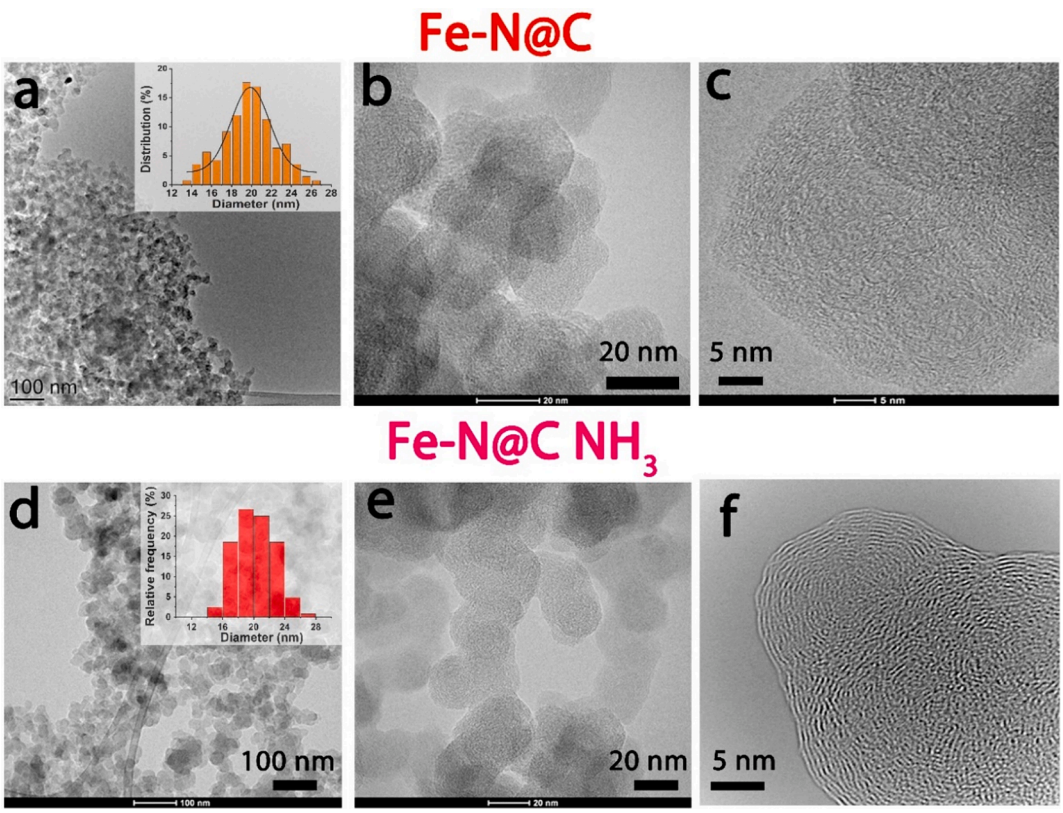

Fig. 2. Advanced electron transmission microscopy characterization of single iron-site catalyst supported on carbon matrixes: (a-b) TEM images and inset of particle size distribution for **Fe-N@C** sample; (c) High-resolution TEM (HR-TEM) of the **Fe-N@C** sample; (d-e) TEM images and inset of particle size distribution for the **Fe-N@C-NH$_3$** sample; (f) High-resolution TEM (HR-TEM) of the **Fe-N@C-NH$_3$** sample.

STEM images also confirmed the presence of atomically dispersed Fe atoms in the form of brighter spots with higher Z number (Fig. 3b-3c and 3f-3 g). The presence of N and Fe was additionally confirmed by Electron Energy Loss Spectroscopy (EELS) and the specific identification of the Fe-K and N-K absorption edges, thereby suggesting the coordinated structure of Fe and N in both samples (Fig. 3d and 3 h). Based in the microwave plasma atomic emission spectroscopy (MP-AES) analysis, the Fe content was 0.11 wt% and 0.15 wt% for **Fe-N@C** and **Fe-N@C-NH$_3$**, respectively (Table S1).

To tune the chemical state of doped nitrogen and increase the stability of the catalysts [54,58], the **Fe-N@C** and **Fe-N@C-NH$_3$** samples were further subjected to an activation post-treatment to give the final catalysts **Fe-N@C (2HT)** and **Fe-N@C-NH$_3$ (2HT)**. TEM and HAADF-STEM-EDX advanced characterization confirmed that both samples kept the same morphology and the presence of a homogeneous distribution of Fe. STEM images also corroborated the absence of Fe-based clusters, NPs or bigger aggregates (Fig. S2c-S2d and S3c-S3d). The content of Fe analysed by ICP revealed that the amount of Fe in the final catalysts remained as 0.10 wt% (Table S1). No Fe loss was detected after the acid leaching process. This Fe loading was significantly smaller than the values usually reported for Fe/N/C, typically around 2.5–0.6 wt% [16]. Such a low value suggests the formation of atomically dispersed Fe sites, without the formation of non-desired secondary iron phases such as nanoparticles of metallic iron, iron carbides/nitrides and or iron oxides, usually found in Fe/N/C catalysts obtained from thermal treatments of Fe, N and C precursors.

To further study the bulk structural features of all samples, X-ray diffraction (XRD) and Raman spectroscopy analysis were carried out. XRD patterns of all samples showed a broad peak around $2\theta = 25°$ indexed to the (002) plane and a small peak at 44° corresponding to (100) plane of graphitic carbon (Fig. S4a) [56,59]. The intensity of the peaks became stronger with the activation processes, indicating that upon heating at 900 °C the graphitic nature of the catalysts increased [60,61]. No additional peaks could be detected in the pattern, even in the initial samples, demonstrating that crystalline Fe-based inorganic nanoparticles were not formed during the laser pyrolysis process. Raman spectra displayed two broad peaks at about 1347 and 1579 cm^{-1}, which can be assigned to the D band and G band, respectively (see Fig. S4b). D band is related to the breaking of symmetry caused by structural disorders and defects, whereas the G band represents the in-plane tangential stretching vibration mode (E_{2g}) of the graphite sheet [62,63]. The position of both peaks was analogous for all the samples. The ratio D and G band intensities (I_D/I_G) slightly decreased from 1.02, 1.00, 0.99 to 0.98 for **Fe-N@C**, **Fe-N@C-NH$_3$**, **Fe-N@C(2HT),** and **Fe-N@C-NH$_3$(2HT)**, respectively. The decrease in the I_D/I_G ratios suggests that the carbon structure becomes more ordered and graphitic [64,65]. Nevertheless, the differences in the ratios were not conclusive enough to establish clear differences among the samples by this spectroscopic technique.

The surface properties of the prepared samples were determined by nitrogen isotherms, as shown in Figure S5 all the samples revealed type IV isotherms characteristic for microporous and mesoporous materials [66]. The Brunauer-Emmett-Teller (BET) surface areas of **Fe-N@C**, **Fe-N@C-NH$_3$**, **Fe-N@C(2HT)** and **Fe-N@C-NH$_3$(2HT)** were determined to be 79, 20, 201 and 298 m^2g^{-1}, respectively. Table S2 summarized the BET surface area, pore volume and average pore diameter of all the prepared samples. **Fe-N@C** (79 m^2g^{-1}) shows higher surface area than **Fe-N@C-NH$_3$** (20 m^2g^{-1}), and the surface areas increase further after the activation process, being 201 m^2g^{-1} for **Fe-N@C(2HT)** and 298 m^2g^{-1} for **Fe-N@C-NH$_3$(2HT)**. A similar trend was observed for the total volume (see Table S2), suggesting that during the activation process carbon/nitrogen-containing gaseous species could be formed and further be eliminated under vacuum. The small contribution of micropores (Table S2) could be attributed to a major presence of carbon

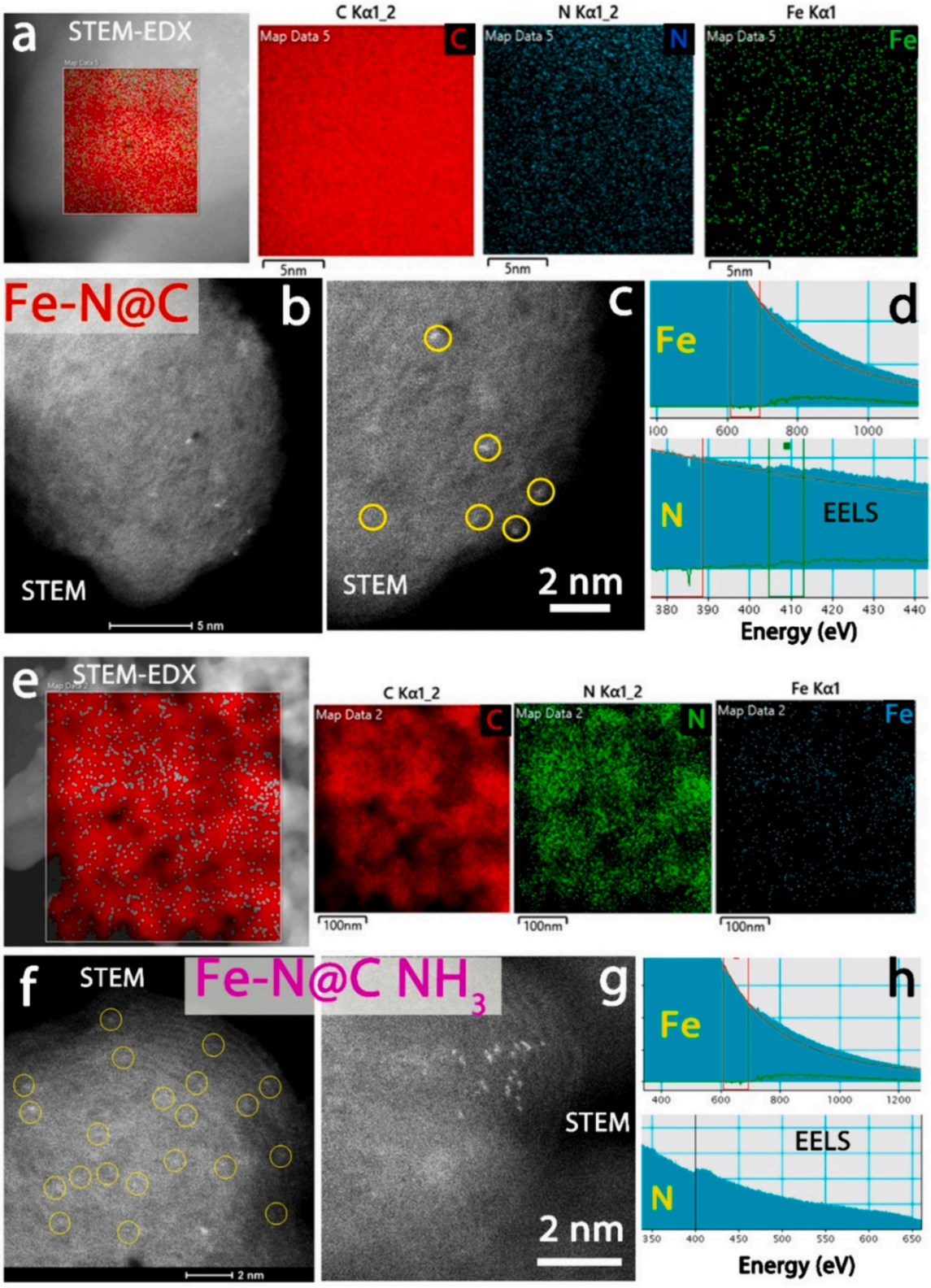

Fig. 3. High-angle annular dark-field scanning transmission electron microscopy (HAADF-STEM) and energy-dispersive X-ray spectroscopy (EDS) analysis of single iron-site catalyst supported on carbon matrixes: (a) STEM-EDX mapping of C, N, and Fe on **Fe-N@C**; (b-c) HAADF-STEM images of the **Fe-N@C** sample with the presence of Fe SAs highlighted by yellow circles; (d) EELS spectroscopy corresponding to the N-K and Fe-K edges in the **Fe-N@C** sample; (e) STEM-EDX mapping of C, N, and Fe on **Fe-N@C-NH$_3$**; (f-g) HAADF-STEM images of the **Fe-N@C-NH$_3$** sample with the presence of Fe SAs highlighted by yellow circles; (h) EELS spectroscopy corresponding to the N-K and Fe-K edges in the **Fe-N@C-NH$_3$** sample. (For interpretation of the references to colour in this figure legend, the reader is referred to the web version of this article.)

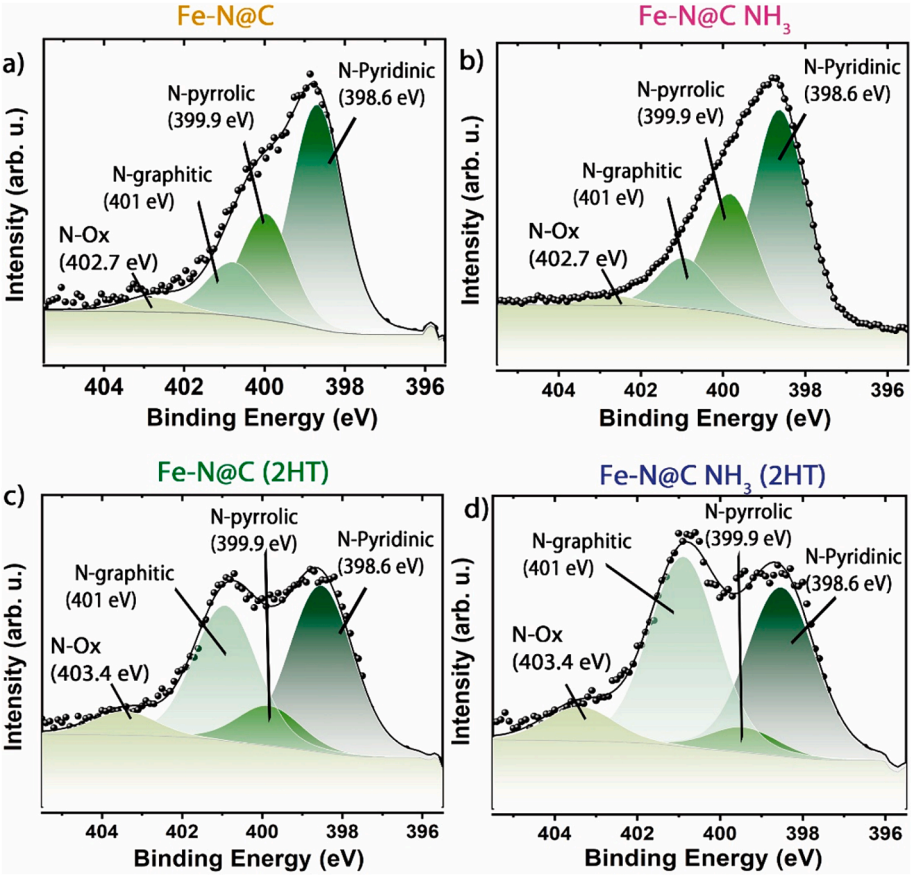

Fig. 4. X-ray photoemission spectra corresponding to the N1s core-level region for samples (a) Fe-N@C, (b) Fe-N@C-NH_3, (c) Fe-N@C (2HT) and (d) Fe-N@C-NH_3 (2HT).

framework defects [67]. Therefore, the higher surface area and pore volume of **Fe-N@C-NH_3(2HT)**, the more effective exposure of active sites and the lower transport resistance of reactants to the active sites, leading to improve ORR activity.

The surface composition of the prepared catalysts was investigated by X-ray photoelectron spectroscopy (XPS). XP survey scans revealed the presence of XP peaks corresponding to the C1s, N1s and O1s regions and no clear contributions in the Fe regions (Figure S6). Table S1 shows the atomic composition obtained from XPS for all samples, including the Fe content, which was determined by MP-AES. The main differences between samples was associated to the N contents. Among the as prepared samples, the N content increased from 3.1 wt% (**Fe-N@C**) to 18.3 wt% (**Fe-N@C-NH_3**), when an extra NH_3 flow was co-fed during the synthesis Comparing the nitrogen content of the initial samples (**Fe-N@C** and **Fe-N@C-NH_3**) with the corresponding to the final catalysts (**Fe-N@C(2HT)** and **Fe-N@C-NH_3(2HT)**) it decreased three times after the activation process.

The introduction of the extra NH_3 ambient could generate C/N-containing gaseous species [38,68], which finally could be evacuated by the vacuum line. The fitting analysis of the N species by XPS (Fig. 4) revealed the coexistence of N-pyridinic (≈ 398.5 eV), N-pyrrolic (≈ 399.9 eV), N-graphitic (≈ 401.6 eV), and some minor contributions associated to N-oxygenated moieties (≈ 402.7–403.4 eV) [44,69,70]. The peak at 398.5 eV may partly contribute to Fe-N owing to the similar binding energies between N-pyridinic and N-Fe [71]. The relative percentage of the different nitrogen species for N1s and the fitting parameters are summarized in Table S3. The relative amount of nitrogen bonding configurations changed significantly after the activation process. As shown in Fig. 4 and Table S3, **Fe-N@C(2HT)** and **Fe-N@C-NH_3(2HT)** contained much higher N-graphitic content than the initial catalysts (**Fe-N@C** and **Fe-N@C-NH_3**), in agreement with the trends displayed by Raman spectroscopy (Fig. S4b). This should be also closely related to the increment of graphitization degree caused by the post treatment at 900 °C. After the thermal activation both N-pyridinic and N-pyrrolic were prone to conversion towards the more thermodynamically stable N-graphitic state [72]. The increase in the N-graphitic fraction may contribute to enhance electrical conductivity of **Fe-N@C-NH_3(2HT)** and render more activity in ORR [73].

The XP spectra of the C1s region (see Figure S7) detected sp^2 and sp^3 C at around 284.6 eV, and minor contributions at around 285.9 eV and 287.7 eV ascribed to different bonding of carbon with nitrogen or oxygen in all samples [44,70,74]. The relative percentage of the different carbon species for C1s are summarized in Table S4. As expected, the increasing intercalation of N atoms induced a major presence of peaks at 285.5 eV (C-N) (Figure S7 and Table S4). The enhanced graphitization degree of the initial catalysts after activation process (**Fe-N@C(2HT)** and **Fe-N@C-NH_3(2HT)**) was corroborated by the increased (π-π^*) graphitic shake-up satellite contribution (Table S4). The heat treatment at 900 °C during the activation process in the presence of Fe, certainly suggests a better graphitization along with the increase in sp2 hybridization that could be responsible for a better electrical conductivity [60,75].

X-ray absorption near-edge (XANES) and fine structure (EXAFS) measurements unarguably confirmed the individual nature of the Fe sites and ruled out the presence of Fe-Fe bonding species (see Fig. 5, Figure S8 and Table S5). We measured the room temperature spectra in several 0.1 wt% Fe content samples, namely **Fe-N@C, Fe-N@C-NH_3** and **Fe-N@C-NH_3 (2HT)**. We also measured Fe-phthalocyanine (FePc) and a-Fe foil as references. The XANES spectra of three samples and two references are shown in the left panel of Fig. 5. The signal obtained from

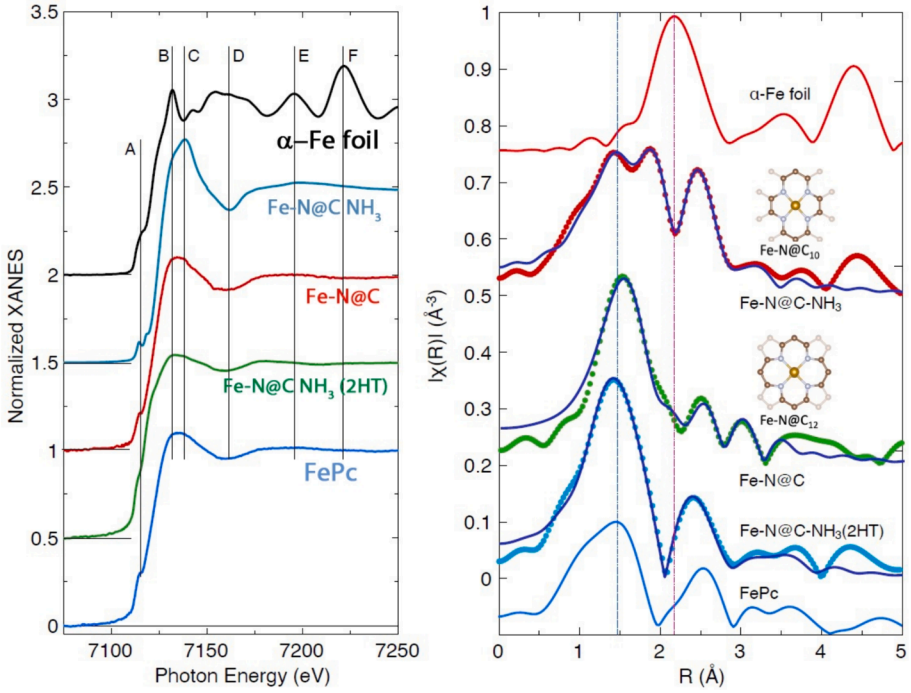

Fig. 5. X-ray absorption near edge (XANES), left panel, and fine structure (EXAFS), right panel, of metallic α-Fe foil, Fe-N@C-NH_3, Fe-N@C, Fe-N@C-NH_3(2HT) and Fe-phthalocyanine (FePc) with the corresponding theoretical fittings matching the samples FT.

the metallic α-Fe foil (bcc structure) shows a well-known peak series (labelled A, B, D, E, and F in the Fig. 5). The characteristic first Fe absorption structure (A) and a contribution coincident in energy with B, which are present in every sample, did not allow discriminating (even qualitatively) on either the presence or absence of metallic Fe on the samples. However, D, E and F were fully absent in FePc and Fe-N/C samples. Note that the peak D in α-Fe coincided with a minimum in FePc, which also appeared on the Fe-N/C samples spectra. Inversely, the C peak in FePc, which was present in the three Fe-N@C spectra, coincided with a minimum in α-Fe. Therefore, a fingerprint analysis of the XANES spectra showed that the local structure and the nature of the nearest neighbors around Fe in all the Fe-N/C samples was much closer to FePc than α-Fe, ruling out a significant presence of metallic Fe clusters in our samples.

The same qualitative result was obtained by inspection of the EXAFS results, shown in the right panel of Fig. 5. The main peak appearing in metallic iron EXAFS, which corresponds to the shortest eight-fold Fe-Fe ~ 2.4 Å distance, was essentially absent in the signal from the Fe-N/C samples (Fig. 5, right panel). Moreover, the comparison between the FePc reference and all the Fe-N/C samples showed very similar features. Indeed, **Fe-N@C** and **Fe-N@C-NH_3 (2HT)** spectra particularly resembled the FePc reference, with a main peak attributed to four-fold Fe-N~1.9 Å. **Fe-N@C-NH_3** revealed a more complex distance distribution around the Fe absorber, though no one of the observed contributions could be undoubtedly assigned to metallic-like Fe-Fe nearest neighbors (Fig. 5).

We further analyzed the EXAFS spectra to retrieve quantitative results by fitting the data to different structural models, namely FeN_4C_{12} and FeN_4C_{10} as described in [76]. These models correspond to two slightly different ways to accommodate the FeN_4 unit into the graphitic environment (see the schemes in Fig. 5 and Figure S8). These models were used to generate the initial scattering paths to fit the EXAFS data. An adjustable fraction of metallic Fe was always allowed in the fitting process (Table S5). As shown in Fig. 5, **Fe-N@C** was nicely fitted to the FeN_4C_{12} model (Figure S8), which essentially holds a phthalocyanine-like structure with the outer 4 nitrogen atoms substituted by carbon. The fraction of metallic Fe included by the ARTEMIS software [51] in these fits was always below 0.1 wt%, with the uncertainty bar fully compatible with zero, thereby ruling out the presence of Fe aggregates in the samples.

Fe-N@C-NH_3 and **Fe-N@C-NH_3(2HT)** matched best with a FeN_4C_{10} model (Figure S8 and Table S5), which introduced the FeN_4 square heme-like group within a graphene layer by removing six carbon atoms. This model has 4 nearer- and 4 further away carbon atoms, facilitating the fit of the multiple peak structure of **Fe-N@C-NH_3** with essentially no-metallic Fe contribution. Indeed, the fits including Fe scattering paths reached unphysical results. In any case, the fits suggested the relaxation of the ideal graphene structure around the FeN_4 centers in both samples. It is also noteworthy that the samples prepared with NH_3 better fitted with the FeN_4C_{10}, suggesting that NH_3 and heat treatment helps the SAC centers to be inserted into the graphitic structure. The detailed structural results of the EXAFS fits are tabulated and displayed in the Supplementary Materials (Table S5 and Figure S8).

3.3. Evaluation of the oxygen reduction reaction activity

The blank voltammograms recorded in Ar-saturated electrolytes for the activated samples displayed a quasi-rectangle shape, typical of carbonaceous materials (Figure S9). Fig. 6a-6b showed the ORR polarization curves (background corrected) and the pure kinetic currents obtained for the samples activated after one or two thermal treatments (**Fe-N@C-NH_3 (1HT)** and **Fe-N@C-NH_3 (2HT)**) in acid and alkaline electrolytes, respectively. The polarization curve in alkaline showed a sharp transition between the kinetic and the mass-transport controlled region, actually reaching a plateau current at potentials less positive than 0.6 V. In contrast, in acid electrolyte, a constant declining of the ORR current with the potential was observed, especially with the catalyst subjected to one thermal treatment, **Fe-N@C-NH_3 (1HT)**. This observation, along with the fact that the ORR failed to reach the theoretical limiting current (ca. 6 mA·cm^{-2} at 1600 rpm in acid electrolyte) suggests either a small number of active sites and/or the limited accessibility of O_2 to them, especially in **Fe-N@C-NH_3 (1HT)**. The effect of pH on the ORR activity has been reported for Pt/C and Fe/N/C catalysts [77]. Whereas FeN_xC_y ensembles are the most active ones for the

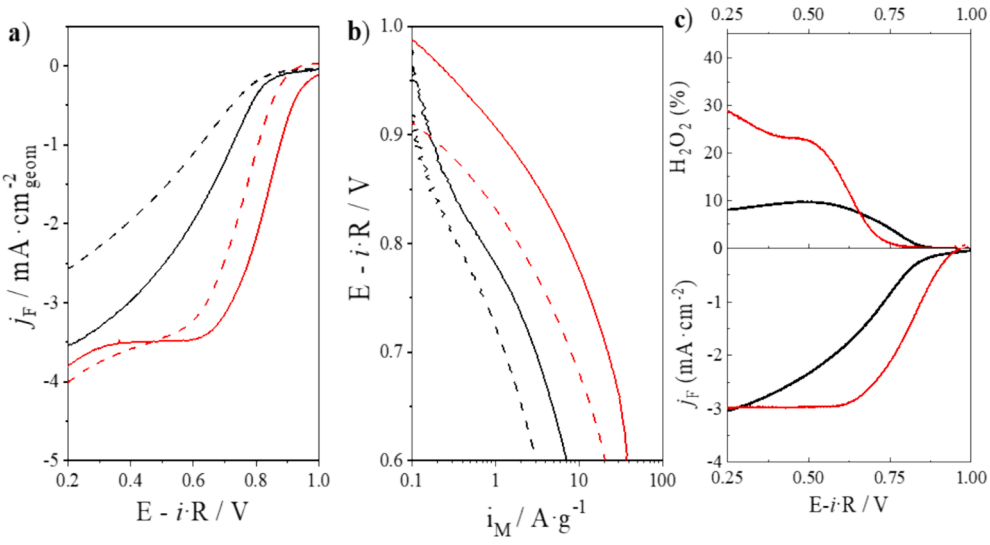

Fig. 6. A) ORR polarization curves of Fe-N@C-NH_3 (1HT) (dash lines) and Fe-N@C-NH_3(2HT) (straight lines) in alkaline electrolyte (red lines) and acid electrolyte (black lines). b) Tafel plots from the curves obtained in (a). c) RRDE measurements, H_2O_2 quantification during ORR. (For interpretation of the references to colour in this figure legend, the reader is referred to the web version of this article.)

ORR in acid electrolyte, other sites, including Fe-free N_xC_y entities and defective carbon layers also display ORR activity in alkaline conditions [34,78,79].

Fe-N@C-NH_3 (1HT) sample showed ORR activity (see Table 1) in both electrolytes, with mass-specific currents (i_m) at 0.8 V of 0.41 and 4.9 $A g_{cat}^{-1}$ in acid and alkaline electrolyte, respectively. E_{onset} values (see Table 1) of 0.85 and 0.90 V in acid and alkaline electrolytes, were obtained. After acid leaching and the second thermal treatment (**Fe-N@C-NH_3 (2HT)**), mass-specific activities of 0.85 and 5.9 $A g_{cat}^{-1}$ in acid and alkaline electrolytes, respectively, were recorded at 0.8 V. Moreover, E_{onset} values shifted to more positive potentials of 0.9 and 1.0 V. The benefits of the second thermal treatment of Fe/N/C catalysts for the ORR have been reported previously [79]. Although the ORR activity in alkaline of **Fe-N@C-NH_3(2HT)** compares well with the literature, (see Table S6), it is still far from that of state-of-the-art Fe/N/C catalyst in acidic conditions (Table S7), especially when compared with recent catalysts based on 2-methyl imidazole or ZIF-8 precursors subjected to several thermal treatments and/or chemical vapor deposition processes [54]. A possible effect of the second thermal treatment would be the development of higher specific surface areas. In fact, we observed the BET areas increased from 201 to 298 $m^2 g^{-1}$ after the second thermal treatment (Table S2). This feature translated into higher electrochemical surface areas (ECSA) values. We obtained ECSA of 410 and 440 $m^2 g_{cat}^{-1}$ for **Fe-N@C-NH_3 (1HT)** and **Fe-N@C-NH_3 (2HT)**, respectively, which represented an increase of ca. 10 % after the second thermal treatment. This feature, can explain the higher ORR activity of the sample subjected to two thermal treatments.

Table 1
Kinetic, mass activity and onset potentials for the ORR with selected catalysts under study in $HClO_4$ 0.1 M and KOH 0.1 M.

	j_k ($mA \cdot cm^{-2}$) @ 0.8 V	i_m ($A \cdot g^{-1}_{cat}$) @ 0.8 V	Tafel slope ($Vdec^{-1}$)	E_{onset} (V) @ −0.1 $mAcm^{-2}$	$E_{1/2}$ (V)
Fe-N@C-NH_3(1HT) (0.1 M $HClO_4$)	0.25	0.41	0.34	0.85	0.65
Fe-N@C-NH_3(2HT) (0.1 M $HClO_4$)	0.51	0.85	0.30	0.90	0.62
Fe-N@C-NH_3(1HT) (0.1 M KOH)	1.88	0.16	0.37	0.90	0.82
Fe-N@C-NH_3(2HT) (0.1 M KOH)	3.52	1.19	0.11	1.01	0.83

The production of H_2O_2, i.e., the reaction pathway (4-electron vs 2-electron) was studied with a RRDE. Fig. 6c shows the evolution of the fraction of H_2O_2 formed with **Fe-N@C-NH_3(2HT)** in 0.1 M $HClO_4$ and 0.1 M KOH. Clearly, the production of H_2O_2 (i.e., the 4-electron pathway) in alkaline electrolyte trebles the production in acidic one. This feature is typical of carbonaceous catalysts subjected to thermal treatments [80] since at high pHs active sites other than FeN_xC_y can play a part in the ORR. For example, quinone groups and N-doped carbon groups displayed ORR activity but via 2 electrons and not directly producing water [81–83].

The durability of the catalysts was also evaluated by applying the accelerated stress tests (AST) described in the Supplementary Materials. Fig. 7 shows the ORR polarization curves recorded before the AST after 5000 and 10,000 cycles in Ar-saturated 0.1 M $HClO_4$ and 0.1 M KOH. It is worth pointing out that $HClO_4$ is a much more aggressive medium than KOH. In acidic electrolyte, Fig. 7a, a clear deactivation was observed after 5000 cycles with the j_F at 0.8 V decreasing from −0.59 to −0.28 $mA \cdot cm^{-2}$, and the limiting current dropping from −3.22 to −2.0 $mA \cdot cm^{-2}$. Noticeably, the activity remained stable when the catalyst was subjected to another 5000 cycles. Besides, the onset potential did not change over the test. Similarly, in alkaline electrolyte (Fig. 7b) the most significant loss of activity occurred within the first 5000 cycles although the reduction was less severe than in acidic electrolyte. The E_{onset} was barely shifted (E_{onset} = 1 V), while a 27 % decrease in current density was observed at 0.8 V. Likewise, the limiting currents decreased after 10,000 cycles, in both the acidic and alkaline electrolytes, indicating the partial loss of active sites during the ORR. Post-mortem analysis of the catalysts recovered indicated a complex chemical environment with the presence of multiple ionic species and also revealed partial corrosion and clustering of Fe species (Figure S11).

As stated above, the ORR activity in alkaline electrolyte compared well with the literature (Table S6). However, ORR acid activity in acid electrolyte remained somehow low (Table S7). This feature can be due to the low Fe loading in the catalysts of ca. 0.1 wt%, (*vide supra*), probably resulting in a small fraction of surface iron sites. In order to confirm this feature, the number of accessible Fe sites (site density SD_{mass}) was

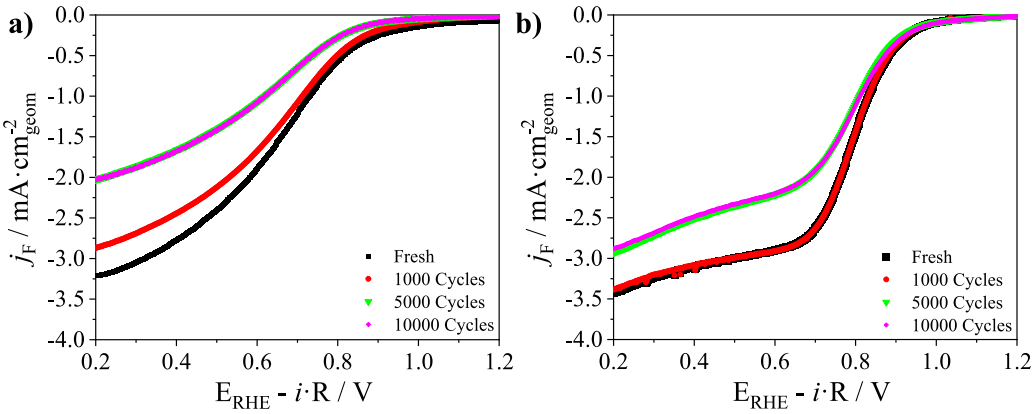

Fig. 7. ORR polarization curves of Fe-N@C-NH_3(2HT) before and after DOE AST in a) Ar-saturated 0.1 M $HClO_4$ and b) Ar-saturated KOH 0.1 M. The ORR was measured at 1600 rpm.

estimated by the electrochemical stripping of NO [47]. To estimate the number of active sites several assumptions were considered: i) one adsorbed NO is reduced per site and ii) NO stripping occurred via a three-electron reduction to produce hydroxylamine, i.e., we used an n = 3 in Equation S8) [37].

SD_{mass} values of $1.36{\cdot}10^{19}$ and $1.22{\cdot}10^{19}$ sites·g^{-1} were obtained for **Fe-N@C-NH_3(1HT)** and **Fe-N@C-NH_3(2HT)**. Note that these values corresponded to Fe loadings of 0.12 and 0.11 wt%, in good agreement with the Fe loading obtained from ICP (*vide supra*). As observed, the second thermal treatment did not entail an increase of the site density. These values were ca. one order of magnitude lower than SD_{mass} values reported recently for the most active FeN_xC_y catalysts in the literature ($1{\cdot}10^{20}$ sites·g^{-1}) [37]. However, the SD_{mass} values obtained for **Fe-N@C-NH_3 (1HT)** and **Fe-N@C-NH_3 (2HT)** compare well with the values reported for similar Fe/N/C catalysts with higher Fe loadings [16]. It is worth to note that previous studies assumed a five-electron process (n = 5 in Equation S8) for the calculation of SD_{mass}, in which case we obtained SD_{mass} values of $8.16{\cdot}10^{18}$ and $7.32{\cdot}10^{18}$ sites·g^{-1} for **Fe-N@C-NH_3 (1HT)** and **Fe-N@C-NH_3 (2HT)**, respectively. These values compare well with SD_{mass} values reported for high-performance ORR catalysts, *e.g.* $8.6{\cdot}10^{18}$ sites·g^{-1} for a polymerized di-amino naphthalene-based catalysts from Imperial College London (ICL), being greater than SD_{mass} reported for two catalysts synthesized via hard templating with fumed silica, one from the University of New Mexico ($6.3{\cdot}10^{18}$ sites·g^{-1}) and another one from Pajarito Powder Inc. ($2.5{\cdot}10^{18}$ sites·g^{-1}) [16].

The turnover frequency (TOF) was calculated from Equation (1) (*vide infra*) by taking into account the difference in the mass kinetic current (i_m) between the unpoisoned and poisoned catalyst at a certain potential (0.8 V vs. RHE in this work), see Figure S12. The Tafel plots and i_m values are shown in Figure S13.

$$TOF\left(electron{\cdot}site^{-1}{\cdot}s^{-1}\right) = \frac{i_{mass}[A{\cdot}g^{-1}]{\cdot}N_A\left[Atom{\cdot}mol^{-1}\right]}{SD_{mass}[sites{\cdot}g^{-1}]{\cdot}F\left[A{\cdot}s{\cdot}mol^{-1}\right]} \quad (1)$$

The TOF values calculated at 0.8 V in the same electrolyte than the one used for the determination of the SD_{mass} for **Fe-N@C-NH_3(1HT)** and **Fe-N@C-NH_3(2HT)** are 0.41 and 0.87 electrons·$site^{-1}$·s^{-1}, respectively. These TOFs were calculated assuming a 5-electron transfer in Eq. S8, in order to compare with reported values. These values are within the range of TOF values reported previously under analogous conditions [47]. In fact, they are higher than the TOF estimated for the ZIF-derived catalyst from CNRS/University of Montpellier (0.65 electrons·$site^{-1}$·s^{-1}) and similar to the polymerized di-amino naphthalene-based catalyst from ICL (0.96 electron·$site^{-1}$·s^{-1} at 0.8 V). The values, however, are still far from the highest TOF recently reported in the literature of 2.75 electrons·$site^{-1}$·s^{-1} (at 0.9 V) for a single atom iron sites (FeN_4) embedded in carbon Fe/N/C catalyst synthesized from ZIF-8 and Fe_2O_3, using thermal treatments and chemical vapor deposition (CVD) steps [36].

4. Conclusions

This study proved that a robust approach to synthesize Fe-N/C single atom catalysts can be obtained by laser-driven pyrolysis of a solution containing iron phthalocyanine and pyridine. Fe single atoms were homogeneously distributed on the N-C matrix without giving rise to unwanted Fe species or aggregates. Advanced microscopy and especially XANES and EXAFS analyses confirmed the isolated nature of the Fe atoms and the resemblance to the Fe-phthalocyanine molecular environment. The catalysts obtained by this synthesis procedure consistently led to Fe contents around 0.1–0.15 wt% in agreement with the site density estimated from electrochemical stripping of NO ($1.3{\cdot}10^{19}$ sites·g^{-1}) and confirming that all the active sites are accessible. Much higher ORR activity and H_2O_2 production were observed in alkaline media than with acidic electrolytes due to the involvement of other active sites apart from the FeN_xC_y in alkaline electrolyte. The catalysts showed good stability, especially in acid electrolyte. The catalysts yielded TOF values (0.87 electrons·$site^{-1}$·s^{-1}) within the range commonly reported for other Fe-N/C catalysts. In conclusion, the versatility of this laser technique and the potential tuning of the feeding precursors paves the way for a controlled and systematic generation of different types of SACs that can help to understand the correlation between structure and electrocatalytic response of these materials.

CRediT authorship contribution statement

Ainhoa Madrid: Validation, Methodology, Investigation, Formal analysis, Data curation. **Álvaro Tolosana-Moranchel:** Visualization, Validation, Methodology, Investigation, Formal analysis, Data curation. **Álvaro García:** Validation, Investigation, Formal analysis, Data curation. **Sergio Rojas:** Writing – review & editing, Writing – original draft, Validation, Supervision, Resources, Project administration, Methodology, Investigation, Funding acquisition, Formal analysis, Data curation, Conceptualization. **Fernando Bartolome:** Writing – review & editing, Validation, Methodology, Formal analysis, Data curation. **Ekaterina Pakrieva:** Validation, Methodology, Investigation. **Laura Simonelli:** Writing – review & editing, Validation, Methodology, Investigation, Formal analysis. **Gema Martinez:** Writing – review & editing, Writing – original draft, Validation, Supervision, Methodology, Investigation, Formal analysis, Data curation, Conceptualization. **Jose L. Hueso:** Writing – review & editing, Validation, Supervision, Investigation, Funding acquisition, Formal analysis, Conceptualization. **Jesus Santamaria:** Writing – review & editing, Writing – original draft, Visualization, Validation, Supervision, Resources, Project administration,

Methodology, Investigation, Funding acquisition, Formal analysis, Data curation, Conceptualization.

Declaration of competing interest

The authors declare that they have no known competing financial interests or personal relationships that could have appeared to influence the work reported in this paper.

Data availability

Data will be made available on request.

Acknowledgements

The authors thank funding from the Spanish Research Agency and MICN/AEI (projects PID2020-114926RB-I00, CNS2022-135911 and PID2020-115159 GB-I00) and from CIBER-BBN and the Government of Aragon (Group T57_23R). Financial support from PID2020-116712RB-C21 funded by MCIN/AEI/10.13039/501100011033 is also acknowledged. We also thank the Consejería de Educación, Juventud y Deporte of the Comunidad de Madrid for the Ayuda Destinada a la Atracción de Talento Investigador (2020-T2/AMB-19927) granted to Álvaro Tolosana Moranchel. The Deputyship for Research & Innovation, Ministry of Education of Saudi Arabia for the project number 341 is also acknowledged. The synthesis of materials has been performed by the Platform of Production of Biomaterials and Nanoparticles of the NANOBIOSIS ICTS, more specifically by the Nanoparticle Synthesis Unit (Unit 9) of the CIBER in Bioengineering, Biomaterials & Nanomedicine (CIBER-BBN). The TEM studies were conducted at the Laboratorio de Microscopias Avanzadas, Instituto de Nanociencia y Materiales de Aragon, Universidad de Zaragoza, Spain. The XAS experiments were performed at the CLAESS beamline of the ALBA synchrotron (proposal number 2022097042) with the support of the ALBA staff. Ayuda CEX2023-001286-S financiada por MICIU/AEI /10.13039/501100011033.

Appendix A. Supplementary data

Supplementary data to this article can be found online at https://doi.org/10.1016/j.cej.2024.155363.

References

[1] F. Chen, X. Jiang, L. Zhang, R. Lang, B. Qiao, Single-atom catalysis: Bridging the homo- and heterogeneous catalysis, Chin. J. Catal. 39 (2018) 893–898.
[2] P. Liu, Y. Zhao, R. Qin, S. Mo, G. Chen, L. Gu, D.M. Chevrier, P. Zhang, Q. Guo, D. Zang, B. Wu, G. Fu, N. Zheng, Photochemical route for synthesizing atomically dispersed palladium catalysts, Science 352 (2016) 797–800.
[3] R. Lang, T. Li, D. Matsumura, S. Miao, Y. Ren, Y.-T. Cui, Y. Tan, B. Qiao, L. Li, A. Wang, X. Wang, T. Zhang, Hydroformylation of Olefins by a Rhodium Single-Atom Catalyst with Activity Comparable to RhCl(PPh3)3, Angew. Chem. Int. Ed. 55 (2016) 16054–16058.
[4] Š. Kment, A. Bakandritsos, I. Tantis, H. Kmentová, Y. Zuo, O. Henrotte, A. Naldoni, M. Otyepka, R.S. Varma, R. Zbořil, Single Atom Catalysts Based on Earth-Abundant Metals for Energy-Related Applications, Chem. Rev. (2024) in press.
[5] A. Wang, J. Li, T. Zhang, Heterogeneous single-atom catalysis, Nat. Rev. Chem. 2 (2018) 65–81.
[6] J. Wang, H. Kong, J. Zhang, Y. Hao, Z. Shao, F. Ciucci, Carbon-based electrocatalysts for sustainable energy applications, Prog. Mater Sci. 116 (2021) 100717.
[7] X. Li, L. Liu, X. Ren, J. Gao, Y. Huang, B. Liu, Microenvironment modulation of single-atom catalysts and their roles in electrochemical energy conversion, Sci. Adv. 6 (2020) eabb6833.
[8] Z.W. Chen, L.X. Chen, C.C. Yang, Q. Jiang, Atomic (single, double, and triple atoms) catalysis: frontiers, opportunities, and challenges, J. Mater. Chem. A 7 (2019) 3492–3515.
[9] S. Das, J. Pérez-Ramírez, J. Gong, N. Dewangan, K. Hidajat, B.C. Gates, S. Kawi, Core–shell structured catalysts for thermocatalytic, photocatalytic, and electrocatalytic conversion of CO2, Chem. Soc. Rev. 49 (2020) 2937–3004.
[10] Y. Chen, S. Ji, C. Chen, Q. Peng, D. Wang, Y. Li, Single-Atom Catalysts: Synthetic Strategies and Electrochemical Applications, Joule 2 (2018) 1242–1264.
[11] J. Liu, H. Zhang, M. Qiu, Z. Peng, M.K.H. Leung, W.-F. Lin, J. Xuan, A review of non-precious metal single atom confined nanomaterials in different structural dimensions (1D–3D) as highly active oxygen redox reaction electrocatalysts, J. Mater. Chem. A 8 (2020) 2222–2245.
[12] Y. Jia, X. Yao, Atom-Coordinated Structure Triggers Selective H2O2 Production, Chem 6 (2020) 548–550.
[13] J. Gao, H.B. Yang, X. Huang, S.-F. Hung, W. Cai, C. Jia, S. Miao, H.M. Chen, X. Yang, Y. Huang, T. Zhang, B. Liu, Enabling Direct H2O2 Production in Acidic Media through Rational Design of Transition Metal Single Atom Catalyst, Chem 6 (2020) 658–674.
[14] L. Fan, P.F. Liu, X. Yan, L. Gu, Z.Z. Yang, H.G. Yang, S. Qiu, X. Yao, Atomically isolated nickel species anchored on graphitized carbon for efficient hydrogen evolution electrocatalysis, Nat. Commun. 7 (2016) 10667.
[15] T.N. Huan, N. Ranjbar, G. Rousse, M. Sougrati, A. Zitolo, V. Mougel, F. Jaouen, M. Fontecave, Electrochemical Reduction of CO2 Catalyzed by Fe-N-C Materials: A Structure-Selectivity Study, ACS Catal. 7 (2017) 1520–1525.
[16] M. Primbs, Y. Sun, A. Roy, D. Malko, A. Mehmood, M.-T. Sougrati, P.-Y. Blanchard, G. Granozzi, T. Kosmala, G. Daniel, P. Atanassov, J. Sharman, C. Durante, A. Kucernak, D. Jones, F. Jaouen, P. Strasser, Establishing reactivity descriptors for platinum group metal (PGM)-free Fe–N–C catalysts for PEM fuel cells, Energ. Environ. Sci. 13 (2020) 2480–2500.
[17] N. Gong, X. Ma, X. Ye, Q. Zhou, X. Chen, X. Tan, S. Yao, S. Huo, T. Zhang, S. Chen, X. Teng, X. Hu, J. Yu, Y. Gan, H. Jiang, J. Li, X.-J. Liang, Carbon-dot-supported atomically dispersed gold as a mitochondrial oxidative stress amplifier for cancer treatment, Nat. Nanotechnol. 14 (2019) 379–387.
[18] S. Gupta, S. Zhao, O. Ogoke, Y. Lin, H. Xu, G. Wu, Engineering Favorable Morphology and Structure of Fe-N-C Oxygen-Reduction Catalysts through Tuning of Nitrogen/Carbon Precursors, ChemSusChem 10 (2017) 774–785.
[19] M.B. Gawande, P. Fornasiero, R. Zbořil, Carbon-Based Single-Atom Catalysts for Advanced Applications, ACS Catal. 10 (2020) 2231–2259.
[20] B. Qiao, A. Wang, X. Yang, L.F. Allard, Z. Jiang, Y. Cui, J. Liu, J. Li, T. Zhang, Single-atom catalysis of CO oxidation using Pt1/FeOx, Nat. Chem. 3 (2011) 634–641.
[21] X. Guo, G. Fang, G. Li, H. Ma, H. Fan, L. Yu, C. Ma, X. Wu, D. Deng, M. Wei, D. Tan, R. Si, S. Zhang, J. Li, L. Sun, Z. Tang, X. Pan, X. Bao, Direct, Nonoxidative Conversion of Methane to Ethylene, Aromatics, and Hydrogen, Science 344 (2014) 616–619.
[22] S. Sun, G. Zhang, N. Gauquelin, N. Chen, J. Zhou, S. Yang, W. Chen, X. Meng, D. Geng, M.N. Banis, R. Li, S. Ye, S. Knights, G.A. Botton, T.-K. Sham, X. Sun, Single-atom Catalysis Using Pt/Graphene Achieved through Atomic Layer Deposition, Sci. Rep. 3 (2013) 1775.
[23] F.R. Lucci, J. Liu, M.D. Marcinkowski, M. Yang, L.F. Allard, M. Flytzani-Stephanopoulos, E.C.H. Sykes, Selective hydrogenation of 1,3-butadiene on platinum–copper alloys at the single-atom limit, Nat. Commun. 6 (2015) 8550.
[24] M. Moses-DeBusk, M. Yoon, L.F. Allard, D.R. Mullins, Z. Wu, X. Yang, G. Veith, G. M. Stocks, C.K. Narula, CO Oxidation on Supported Single Pt Atoms: Experimental and ab Initio Density Functional Studies of CO Interaction with Pt Atom on θ-Al2O3(010) Surface, J. Am. Chem. Soc. 135 (2013) 12634–12645.
[25] T. Sun, S. Zhao, W. Chen, D. Zhai, J. Dong, Y. Wang, S. Zhang, A. Han, L. Gu, R. Yu, X. Wen, H. Ren, L. Xu, C. Chen, Q. Peng, D. Wang, Y. Li, Single-atomic cobalt sites embedded in hierarchically ordered porous nitrogen-doped carbon as a superior bifunctional electrocatalyst, Proc. Natl. Acad. Sci. 115 (2018) 12692–12697.
[26] Z. Li, Y. Chen, S. Ji, Y. Tang, W. Chen, A. Li, J. Zhao, Y. Xiong, Y. Wu, Y. Gong, T. Yao, W. Liu, L. Zheng, J. Dong, Y. Wang, Z. Zhuang, W. Xing, C.-T. He, C. Peng, W.-C. Cheong, Q. Li, M. Zhang, Z. Chen, N. Fu, X. Gao, W. Zhu, J. Wan, J. Zhang, L. Gu, S. Wei, P. Hu, J. Luo, J. Li, C. Chen, Q. Peng, X. Duan, Y. Huang, X.-M. Chen, D. Wang, Y. Li, Iridium single-atom catalyst on nitrogen-doped carbon for formic acid oxidation synthesized using a general host–guest strategy, Nat. Chem. 12 (2020) 764–772.
[27] P. Yin, T. Yao, Y. Wu, L. Zheng, Y. Lin, W. Liu, H. Ju, J. Zhu, X. Hong, Z. Deng, G. Zhou, S. Wei, Y. Li, Single Cobalt Atoms with Precise N-Coordination as Superior Oxygen Reduction Reaction Catalysts, Angew. Chem. Int. Ed. 55 (2016) 10800–10805.
[28] C. Zhao, X. Dai, T. Yao, W. Chen, X. Wang, J. Wang, J. Yang, S. Wei, Y. Wu, Y. Li, Ionic Exchange of Metal-Organic Frameworks to Access Single Nickel Sites for Efficient Electroreduction of CO2, J. Am. Chem. Soc. 139 (2017) 8078–8081.
[29] X. Wang, W. Chen, L. Zhang, T. Yao, W. Liu, Y. Lin, H. Ju, J. Dong, L. Zheng, W. Yan, X. Zheng, Z. Li, X. Wang, J. Yang, D. He, Y. Wang, Z. Deng, Y. Wu, Y. Li, Uncoordinated Amine Groups of Metal-Organic Frameworks to Anchor Single Ru Sites as Chemoselective Catalysts toward the Hydrogenation of Quinoline, J. Am. Chem. Soc. 139 (2017) 9419–9422.
[30] Y. Chen, S. Ji, Y. Wang, J. Dong, W. Chen, Z. Li, R. Shen, L. Zheng, Z. Zhuang, D. Wang, Y. Li, Isolated Single Iron Atoms Anchored on N-Doped Porous Carbon as an Efficient Electrocatalyst for the Oxygen Reduction Reaction, Angewandte Chemie International Edition 56 (2017) 6937–6941.
[31] W. Liu, L. Zhang, X. Liu, X. Liu, X. Yang, S. Miao, W. Wang, A. Wang, T. Zhang, Discriminating Catalytically Active FeNx Species of Atomically Dispersed Fe–N–C Catalyst for Selective Oxidation of the C-H Bond, J. Am. Chem. Soc. 139 (2017) 10790–10798.
[32] W. Liu, L. Zhang, W. Yan, X. Liu, X. Yang, S. Miao, W. Wang, A. Wang, T. Zhang, Single-atom dispersed Co–N–C catalyst: structure identification and performance for hydrogenative coupling of nitroarenes, Chem. Sci. 7 (2016) 5758–5764.
[33] C. Domínguez, F.J. Pérez-Alonso, M.A. Salam, S.A. Al-Thabaiti, M.A. Peña, F. J. García-García, L. Barrio, S. Rojas, Repercussion of the carbon matrix for the activity and stability of Fe/N/C electrocatalysts for the oxygen reduction reaction, Appl Catal B 183 (2016) 185–196.
[34] Á. García, L. Pascual, P. Ferrer, D. Gianolio, G. Held, D.C. Grinter, M.A. Peña, M. Retuerto, S. Rojas, Study of the evolution of FeNxCy and Fe3C species in Fe/N/C

catalysts during the oxygen reduction reaction in acid and alkaline electrolyte, J. Power Sources 490 (2021) 229487.
[35] L. Lin, Q. Zhu, A.-W. Xu, Noble-Metal-Free Fe–N/C Catalyst for Highly Efficient Oxygen Reduction Reaction under Both Alkaline and Acidic Conditions, J. Am. Chem. Soc. 136 (2014) 11027–11033.
[36] S. Liu, C. Li, M.J. Zachman, Y. Zeng, H. Yu, B. Li, M. Wang, J. Braaten, J. Liu, H. M. Meyer, M. Lucero, A.J. Kropf, E.E. Alp, Q. Gong, Q. Shi, Z. Feng, H. Xu, G. Wang, D.J. Myers, J. Xie, D.A. Cullen, S. Litster, G. Wu, Atomically dispersed iron sites with a nitrogen–carbon coating as highly active and durable oxygen reduction catalysts for fuel cells, Nat. Energy 7 (2022) 652–663.
[37] L. Jiao, J. Li, L.L. Richard, Q. Sun, T. Stracensky, E. Liu, M.T. Sougrati, Z. Zhao, F. Yang, S. Zhong, H. Xu, S. Mukerjee, Y. Huang, D.A. Cullen, J.H. Park, M. Ferrandon, D.J. Myers, F. Jaouen, Q. Jia, Chemical vapour deposition of Fe–N–C oxygen reduction catalysts with full utilization of dense Fe–N4 sites, Nat. Mater. 20 (2021) 1385–1391.
[38] C. Spreafico, D. Russo, R. Degl'Innocenti, Laser pyrolysis in papers and patents, J. Intell. Manuf. 33 (2022) 353–385.
[39] G. Martinez, V. Sebastian, J.L. Hueso, Alternative methodologies for the production of nanomaterials based on microfluidics and laser pyrolysis technologies, in: P. W. Ahmed (Ed.), Manufacturing Nanostructures, One Central Press, 2015.
[40] N. Herlin-Boime, Y. Leconte, D. Porterat, C. Reynaud, O. Sublemontier, Laser pyrolysis: a versatile method to produce nanopowder, Actual. Chim. (2008) 14–15.
[41] A.V. Kabashin, A. Singh, M.T. Swihart, I.N. Zavestovskaya, P.N. Prasad, Laser-Processed Nanosilicon: A Multifunctional Nanomaterial for Energy and Healthcare, ACS Nano 13 (2019) 9841–9867.
[42] J.H. Yeon, S.J. Park, I. Choi, M. Choi, Generation of carbon nano-onions by laser irradiation of gaseous hydrocarbons for high durability catalyst support in proton exchange membrane fuel cells, Journal of Industrial and Engineering Chemistry 80 (2019) 65–73.
[43] A. Malumbres, G. Martinez, R. Mallada, J.L. Hueso, O. Bomati-Miguel, J. Santamaria, Continuous production of iron-based nanocrystals by laser pyrolysis. Effect of operating variables on size, composition and magnetic response, Nanotechnology 24 (2013).
[44] N. Mas, J.L. Hueso, G. Martinez, A. Madrid, R. Mallada, M. Carmen Ortega-Liebana, C. Bueno-Alejo, J. Santamaria, Laser-Driven Direct Synthesis of Carbon Nanodots and Application as Sensitizers for Visible-Light Photocatalysis, Carbon 156 (2020) 453–462.
[45] A. Madrid, G. Martinez, F. Hornos, J. Bonet-Aleta, E. Calvo, A. Lozano, J.L. Hueso, Laser-induced tuning of carbon nanosensitizers to maximize nitrogen doping and reactive oxygen species production in the visible range, Catal. Today 422 (2023) 114214.
[46] H.A. Gasteiger, S.S. Kocha, B. Sompalli, F.T. Wagner, Activity benchmarks and requirements for Pt, Pt-alloy, and non-Pt oxygen reduction catalysts for PEMFCs, Appl Catal B 56 (2005) 9–35.
[47] D. Malko, A. Kucernak, T. Lopes, In situ electrochemical quantification of active sites in Fe–N/C non-precious metal catalysts, Nat. Commun. 7 (2016) 13285.
[48] L. Simonelli, C. Marini, W. Olszewski, M. Avila Perez, N. Ramanan, G. Guilera, V. Cuartero, K. Klementiev, CLÆSS: The hard X-ray absorption beamline of the ALBA CELLS synchrotron, Cogent Physics 3 (2016) 1231987.
[49] D.E. Sayers, B. B.A, in: P. Koningsberger (Ed.), X-Ray Absorption: Principles, Applications, Techniques of EXAFS, SEXAFS and XANES, Wiley, New York, 1988.
[50] B.T. Teo, EXAFS: Basic Principles and Data Analysis, Springer, 1986.
[51] B. Ravel, M. Newville, ATHENA, ARTEMIS, HEPHAESTUS: data analysis for X-ray absorption spectroscopy using IFEFFIT, J. Synchrotron Radiat. 12 (2005) 537–541.
[52] B. Ravel, Quantitative EXAFS analysis in X-Ray Absorption and X-Ray Emission Spectroscopy: Theory and Applications, John Wiley & Son, 2016.
[53] J.J. Rehr, R.C. Albers, Theoretical approaches to x-ray absorption fine structure, Rev. Mod. Phys. 72 (2000) 621–654.
[54] M. Ferrandon, A.J. Kropf, D.J. Myers, K. Artyushkova, U. Kramm, P. Bogdanoff, G. Wu, C.M. Johnston, P. Zelenay, Multitechnique Characterization of a Polyaniline–Iron–Carbon Oxygen Reduction Catalyst, J. Phys. Chem. C 116 (2012) 16001–16013.
[55] H.T. Chung, J.H. Won, P. Zelenay, Active and stable carbon nanotube/nanoparticle composite electrocatalyst for oxygen reduction, Nat. Commun. 4 (2013) 1922.
[56] Z.Q. Li, C.J. Lu, Z.P. Xia, Y. Zhou, Z. Luo, X-ray diffraction patterns of graphite and turbostratic carbon, Carbon 45 (2007) 1686–1695.
[57] Y. Chang, F. Hong, C. He, Q. Zhang, J. Liu, Nitrogen and Sulfur Dual-Doped Non-Noble Catalyst Using Fluidic Acrylonitrile Telomer as Precursor for Efficient Oxygen Reduction, Adv. Mater. 25 (2013) 4794–4799.
[58] D. Xia, X. Yang, L. Xie, Y. Wei, W. Jiang, M. Dou, X. Li, J. Li, L. Gan, F. Kang, Direct Growth of Carbon Nanotubes Doped with Single Atomic Fe–N4 Active Sites and Neighboring Graphitic Nitrogen for Efficient and Stable Oxygen Reduction Electrocatalysis, Adv. Funct. Mater. 29 (2019) 1906174.
[59] R. Li, Z. Wei, X. Gou, Nitrogen and Phosphorus Dual-Doped Graphene/Carbon Nanosheets as Bifunctional Electrocatalysts for Oxygen Reduction and Evolution, ACS Catal. 5 (2015) 4133–4142.
[60] M.Y. Song, D.-S. Yang, K.P. Singh, J. Yuan, J.-S. Yu, Nitrogen-doped hollow carbon spheres with highly graphitized mesoporous shell: Role of Fe for oxygen evolution reaction, Appl Catal B 191 (2016) 202–208.
[61] N.K. Chaudhari, M.Y. Song, J.-S. Yu, Heteroatom-doped highly porous carbon from human urine, Sci. Rep. 4 (2014) 5221.
[62] D.B. Schuepfer, F. Badaczewski, J.M. Guerra-Castro, D.M. Hofmann, C. Heiliger, B. Smarsly, P.J. Klar, Assessing the structural properties of graphitic and non-graphitic carbons by Raman spectroscopy, Carbon 161 (2020) 359–372.
[63] Z.-S. Wu, W. Ren, L. Xu, F. Li, H.-M. Cheng, Doped Graphene Sheets As Anode Materials with Superhigh Rate and Large Capacity for Lithium Ion Batteries, ACS Nano 5 (2011) 5463–5471.
[64] J. Sun, S.E. Lowe, L. Zhang, Y. Wang, K. Pang, Y. Wang, Y. Zhong, P. Liu, K. Zhao, Z. Tang, H. Zhao, Ultrathin Nitrogen-Doped Holey Carbon@Graphene Bifunctional Electrocatalyst for Oxygen Reduction and Evolution Reactions in Alkaline and Acidic Media, Angew. Chem. Int. Ed. 57 (2018) 16511–16515.
[65] K. Yuan, X. Zhuang, H. Fu, G. Brunklaus, M. Forster, Y. Chen, X. Feng, U. Scherf, Two-Dimensional Core-Shelled Porous Hybrids as Highly Efficient Catalysts for the Oxygen Reduction Reaction, Angew. Chem. Int. Ed. 55 (2016) 6858–6863.
[66] M. Thommes, Physical Adsorption Characterization of Nanoporous Materials, Chem. Ing. Tech. 82 (2010) 1059–1073.
[67] Y. Jiang, L. Yang, T. Sun, J. Zhao, Z. Lyu, O. Zhuo, X. Wang, Q. Wu, J. Ma, Z. Hu, Significant Contribution of Intrinsic Carbon Defects to Oxygen Reduction Activity, ACS Catal. 5 (2015) 6707–6712.
[68] F. Jaouen, F. Charreteur, J.P. Dodelet, Fe-Based Catalysts for Oxygen Reduction in PEMFCs: Importance of the Disordered Phase of the Carbon Support, J. Electrochem. Soc. 153 (2006) A689.
[69] D. Long, W. Li, L. Ling, J. Miyawaki, I. Mochida, S.-H. Yoon, Preparation of Nitrogen-Doped Graphene Sheets by a Combined Chemical and Hydrothermal Reduction of Graphene Oxide, Langmuir 26 (2010) 16096–16102.
[70] J.L. Hueso, J.P. Espinos, A. Caballero, J. Cotrino, A.R. Gonzalez-Elipe, XPS investigation of the reaction of carbon with NO, O_2, N_2 and H_2O plasmas, Carbon 45 (2007) 89–96.
[71] Z.-Y. Wu, X.-X. Xu, B.-C. Hu, H.-W. Liang, Y. Lin, L.-F. Chen, S.-H. Yu, Iron Carbide Nanoparticles Encapsulated in Mesoporous Fe-N-Doped Carbon Nanofibers for Efficient Electrocatalysis, Angew. Chem. Int. Ed. 54 (2015) 8179–8183.
[72] S. van Dommele, A. Romero-Izquirdo, R. Brydson, K.P. de Jong, J.H. Bitter, Tuning nitrogen functionalities in catalytically grown nitrogen-containing carbon nanotubes, Carbon 46 (2008) 138–148.
[73] J. Campos-Delgado, I.O. Maciel, D.A. Cullen, D.J. Smith, A. Jorio, M.A. Pimenta, H. Terrones, M. Terrones, Chemical Vapor Deposition Synthesis of N-, P-, and Si-Doped Single-Walled Carbon Nanotubes, ACS Nano 4 (2010) 1696–1702.
[74] D. Bar-Tow, E. Peled, L. Burstein, A Study of Highly Oriented Pyrolytic Graphite as a Model for the Graphite Anode in Li-Ion Batteries, J. Electrochem. Soc. 146 (1999) 824.
[75] D.-S. Yang, M.Y. Song, K.P. Singh, J.-S. Yu, The role of iron in the preparation and oxygen reduction reaction activity of nitrogen-doped carbon, Chem. Commun. 51 (2015) 2450–2453.
[76] T. Lim, G.Y. Jung, J.H. Kim, S.O. Park, J. Park, Y.-T. Kim, S.J. Kang, H.Y. Jeong, S. K. Kwak, S.H. Joo, Atomically dispersed Pt–N4 sites as efficient and selective electrocatalysts for the chlorine evolution reaction, Nat. Commun. 11 (2020) 412.
[77] N. Ramaswamy, S. Mukerjee, Fundamental Mechanistic Understanding of Electrocatalysis of Oxygen Reduction on Pt and Non-Pt Surfaces: Acid versus Alkaline Media, Advances in Physical Chemistry 2012 (2012) 491604.
[78] C. Domínguez, F.J. Pérez-Alonso, J.L. Gómez de la Fuente, S.A. Al-Thabaiti, S. N. Basahel, A.O. Alyoubi, A.A. Alshehri, M.A. Peña, S. Rojas, Influence of the electrolyte for the oxygen reduction reaction with Fe/N/C and Fe/N/CNT electrocatalysts, J. Power Sources 271 (2014) 87–96.
[79] Á. García, T. Haynes, M. Retuerto, P. Ferrer, L. Pascual, M.A. Peña, M. Abdel Salam, M. Mokhtar, D. Gianolio, S. Rojas, Effect of the Thermal Treatment of Fe/N/C Catalysts for the Oxygen Reduction Reaction Synthesized by Pyrolysis of Covalent Organic Frameworks, Ind. Eng. Chem. Res. 60 (2021) 18759–18769.
[80] H.W. Kim, H. Park, J.S. Roh, J.E. Shin, T.H. Lee, L. Zhang, Y.H. Cho, H.W. Yoon, V. J. Bukas, J. Guo, H.B. Park, T.H. Han, B.D. McCloskey, Carbon Defect Characterization of Nitrogen-Doped Reduced Graphene Oxide Electrocatalysts for the Two-Electron Oxygen Reduction Reaction, Chem. Mater. 31 (2019) 3967–3973.
[81] F. Mirkhalaf, K. Tammeveski, D.J. Schiffrin, Substituent effects on the electrocatalytic reduction of oxygen on quinone-modified glassy carbon electrodes, PCCP 6 (2004) 1321–1327.
[82] N.R. Sahraie, U.I. Kramm, J. Steinberg, Y. Zhang, A. Thomas, T. Reier, J.-P. Paraknowitsch, P. Strasser, Quantifying the density and utilization of active sites in non-precious metal oxygen electroreduction catalysts, Nat. Commun. 6 (2015) 8618.
[83] S. Yang, A. Verdaguer-Casadevall, L. Arnarson, L. Silvioli, V. Čolić, R. Frydendal, J. Rossmeisl, I. Chorkendorff, I.E.L. Stephens, Toward the Decentralized Electrochemical Production of H2O2: A Focus on the Catalysis, ACS Catal. 8 (2018) 4064–4081.